Structural and energetic properties of molecular Coulomb crystals in a surface-electrode ion trap

2015 New J. Phys. 17 045008

(http://iopscience.iop.org/1367-2630/17/4/045008)

New Journal of Physics
The open access journal at the forefront of physics

Deutsche Physikalische Gesellschaft DPG
IOP Institute of Physics

Published in partnership with: Deutsche Physikalische Gesellschaft and the Institute of Physics

OPEN ACCESS

RECEIVED
5 December 2014

REVISED
20 February 2015

ACCEPTED FOR PUBLICATION
12 March 2015

PUBLISHED
16 April 2015

PAPER

Structural and energetic properties of molecular Coulomb crystals in a surface-electrode ion trap

A Mokhberi and S Willitsch

Department of Chemistry, University of Basel, Klingelbergstrasse 80, 4056 Basel, Switzerland

E-mail: stefan.willitsch@unibas.ch

Keywords: surface electrode ion traps, cold molecules, Coulomb crystals, sympathetic cooling

Abstract

Cold molecular ions are of great interest for applications in cold collision studies, chemistry, precision spectroscopy and quantum technologies. In this context, sympathetic cooling of molecular ions by the interaction with laser-cooled atomic ions is a powerful method to cool their translational motion and achieve translational temperatures in the millikelvin range. Recently, we implemented this method in a surface-electrode ion trap. The flexibility in shaping the trapping potentials offered by the surface-electrode structure enabled us to generate planar bicomponent Coulomb crystals and spatially separate the molecular from the atomic ions. Here, we present a detailed description of the fabrication and simulation of the trap as well as a theoretical and experimental investigation of the structural and energetic properties of the Coulomb crystals obtained in the device. We discuss in more detail the separation of different ion species using static electric fields and explore the effects of trap anharmoncities on the shape of bicomponent crystals.

1. Introduction

The technology for preparing and controlling cold molecules and molecular ions has made impressive progress over the past years [1–3]. The exquisite control of the internal and external degrees of freedom of the molecules which can be achieved to date paves the way for new applications in quantum computation [4, 5], precision spectroscopy [6, 7], quantum optics [8], mass spectrometry [9, 10], collision studies and cold chemistry [11–14].

The challenges for cooling and detecting molecules generally arise from the lack of closed optical cycles caused by their complex energy-level structures. Therefore, laser cooling and efficient fluorescence detection are limited to a small number of cases [15]. An efficient method applicable to trapped molecular ions is sympathetic cooling of their translational motion through collisions with co-trapped laser-cooled atomic ions leading to the formation of bicomponent Coulomb crystals [1, 16]. This method has been widely used in radiofrequency (RF) traps and is applicable to molecules ranging from diatomics to large biomolecules [1, 17]. It has recently been combined with helium buffer-gas techniques to also achieve cooling of the internal molecular degrees of freedom [18].

On the other hand, the recent miniaturization of ion traps [19] opened up new opportunities for the precise manipulation of trapped particles capitalizing on the strong field gradients achievable in microstructured devices [20], for improving the scalability of traps [21] which is of importance for, e.g., large-scale quantum information processing [22–25], for reducing the size and cost of the experimental apparatus and for the development of multi-functional chip devices [26]. A special variant of miniaturized traps are surface-electrode (SE) RF traps in which all electrodes lie in a plane and the ions are trapped at a certain height above the surface [19, 27]. This new generation of ion traps offers a high flexibility in shaping the trapping potentials based on technological advances in manufacturing and electronics[28]. It is therefore desirable to make these capabilities also available for experiments with molecules and adapt chip-trapping techniques for molecular species.

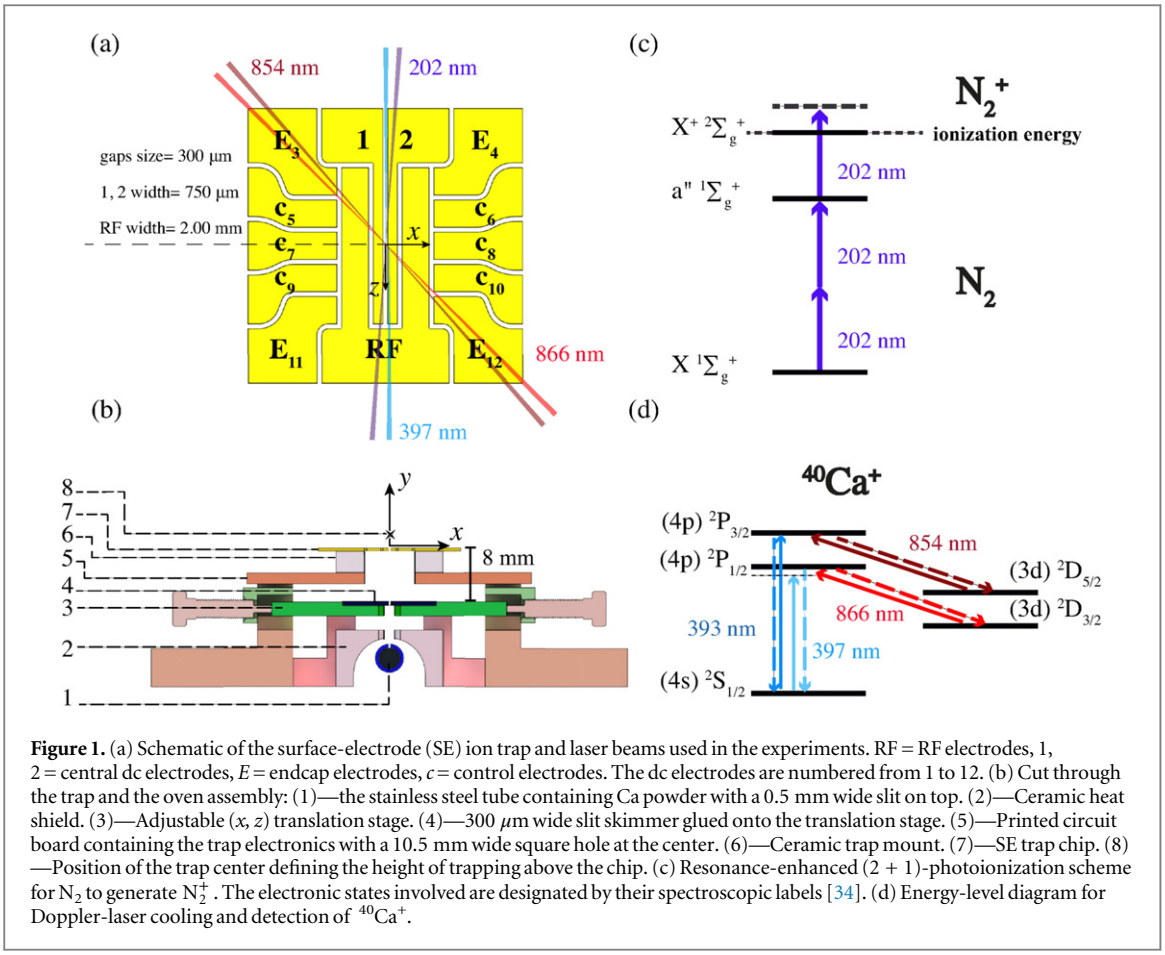

Figure 1. (a) Schematic of the surface-electrode (SE) ion trap and laser beams used in the experiments. RF = RF electrodes, 1, 2 = central dc electrodes, *E* = endcap electrodes, *c* = control electrodes. The dc electrodes are numbered from 1 to 12. (b) Cut through the trap and the oven assembly: (1)—the stainless steel tube containing Ca powder with a 0.5 mm wide slit on top. (2)—Ceramic heat shield. (3)—Adjustable (*x*, *z*) translation stage. (4)—300 μm wide slit skimmer glued onto the translation stage. (5)—Printed circuit board containing the trap electronics with a 10.5 mm wide square hole at the center. (6)—Ceramic trap mount. (7)—SE trap chip. (8)—Position of the trap center defining the height of trapping above the chip. (c) Resonance-enhanced (2 + 1)-photoionization scheme for N_2 to generate N_2^+. The electronic states involved are designated by their spectroscopic labels [34]. (d) Energy-level diagram for Doppler-laser cooling and detection of $^{40}Ca^+$.

Recently, we reported the first sympathetic cooling of molecular ions in a SE trap [29]. In the present paper, we present a detailed account of the fabrication and simulation methods of the trap. We give a characterization of the energetic and structural properties of bicomponent crystals of Ca^+ and N_2^+ ions in the trap using molecular-dynamics (MD) simulation methods and explore the influence of trap anharmonicities on the properties of bicomponent Coulomb crystals.

2. The SE ion trap

2.1. Trap geometry

The SE trap used in the present experiments was based on a six-wire design inspired by the device reported in [30] as already briefly described in our previous article [29]. The trap contained two RF electrodes and twelve electrodes for static (dc) voltages, i.e., six control electrodes, four endcap electrodes and two central electrodes as shown in figure 1(a). The width of the RF and central electrodes amounted to 2.00 mm and 750 μm, respectively. The width of the gaps between the electrodes was 300 μm. The geometry of the trap was optimized using an analytical model [31]. RF voltages applied to the RF electrodes served to provide radial confinement in the (*x*, *y*) plane, while static voltages applied to the twelve dc electrodes were used to confine the ions along the *z* axis (the trap symmetry axis), to shape the trapping potential, to tilt the principal axes of the trap for efficient cooling if required and to compensate excess micromotion [30, 32, 33]. The latter refers to the fast oscillating motion of the ions deriven by the RF field.

2.2. Manufacturing method

The fabrication method of the present SE trap was based on laser cutting the electrodes from a stainless steel foil. The electrodes were machined into the central part of the foil with the edges still connected. The foil was sufficiently thick (0.5 mm) in order to suppress vibrations of the free-standing electrodes. The trap was then electro-polished and coated with a layer of gold with a nominal thickness of 2 μm. Subsequently, the structure was glued onto a ceramic frame with an inner diameter of 10.5 mm. A second laser cut then removed the rim to separate the electrodes, thus generating the final geometry. The trap and its ceramic mount were glued onto a

printed circuit board which contained the trap electronics and was milled out at the center to allow back-side loading of Ca (see below).

2.3. Experimental setup

When loading ions into a trap, it is important to avoid the deposition of material on the electrodes which causes the buildup of stray charges and short circuits in miniaturized traps. We used the central gap (between electrode 1 and 2 in figure 1(a)) for back-side loading of Ca, as illustrated in figure 1(b), to avoid this problem. A beam of Ca atoms was produced by evaporation of metallic Ca from a resistively heated stainless steel tube placed underneath the central trap region. A 300 μm wide slit glued onto a (x, z) translation stage was adjusted underneath the central gap to operate as a skimmer. The atom beam passed through the skimmer, the ceramic mount of the trap and finally the gap between the two central electrodes to reach the trap center where Ca^+ ions were produced by non-resonant photoionization using the same pulsed laser as for N_2 ionization (see below).

The static voltages applied to the trap electrodes were generated by an amplified, LabVIEW-controlled DAC card. RC filters were used to suppress the RF voltages on the dc electrodes and to protect the amplification circuit from the RF voltage (1 nF capacitors were placed inside the vacuum chamber while the accompanying resistors were integrated in the amplifying circuit outside the chamber). The RF drive for the trap was generated by a self-resonating LC circuit [35] with a resonance frequency at $\Omega_{\mathrm{RF}} = 2\pi \times$ 8.0 MHz and 400–600 V amplitude.

For our sympathetic cooling experiments, we chose the prototypical molecular ion N_2^+ (mass 28 amu) [36]. The N_2^+ ions were produced above the surface of the chip by resonance-enhanced $(2 + 1)$-photoionization (REMPI) of N_2 via the $a''^1\Sigma_g^+$ intermediate electronic state (see figure 1(c)) [34]. The N_2 gas was introduced into the vacuum chamber through a leak valve at partial pressures $<6 \times 10^{-9}$ mbar. The frequency-tripled output of a Nd:YAG-pumped pulsed dye laser operating at a wavelength of 202 nm and a pulse energy of 80 μJ was used to carry out REMPI. Doppler laser cooling of Ca^+ ions was achieved by three diode laser beams at 397, 866 and 854 nm addressing the $(4s)^2S_{1/2} \rightarrow (4p)^2P_{1/2}$, $(3d)^2D_{3/2} \rightarrow (4p)^2P_{1/2}$ and $(3d)^2D_{5/2} \rightarrow (4p)^2P_{3/2}$ transitions as depicted in figure 1(d). All lasers propagated parallel to the surface and were superimposed at the trap center 1.82 mm above the chip (see figures 1(a) and (b)). The light scattered by Ca^+ ions during the cooling process was collected by a microscope (magnification 11.5×) and spatially resolved onto an image-intensified CCD camera with a nominal resolution of ≈2 μm. An optical band pass filter (transmission window 340–600 nm) was placed between the microscope and the camera in order to suppress stray light reflected from the surface of the electrodes. The imaging system was set up perpendicular to the trap surface along the y axis and the focus adjusted to the central layer of the crystals in the (x, z) plane.

2.4. Potential modeling

The electrode potentials were calculated by solving the Laplace equation for a three-dimensional model of the trap using finite-element methods (FEM) implemented in the COMSOL Multiphysics software [37] as well as using an analytical model described in [38–40]. The amplitude and the frequency of the RF voltage has been chosen such that the trap depth was maximized while keeping the values of the Mathieu stability parameters [32] small for both N_2^+ and Ca^+ (see below). To find the optimal configuration of static voltages, the parametrization method described in [30, 41] was used. Briefly, a configuration of electrode voltages V leading to desired trap operating conditions was determined by solving the linear equation $KV = B$. Here, K denotes a matrix of coefficients whose elements were computed using least-squares quadratic fits to electrode-potential basis functions $\Phi_{\mathrm{dc},i}$ [42] obtained by solving the Laplace equation for a unit voltage applied to the ith dc electrode. V is an array of independent voltages V_i $(i = 1, \ldots, 12)$ applied to the ith dc electrode. B is an array of potential coefficients corresponding to the desired trap operating condition.

The position of the RF null line where the RF field vanishes was calculated to be 1.82 mm above the surface. In order to calculate the trap depth and the secular motional frequencies of the ions, the adiabatic approximation was used [43]. The total effective trapping potential Φ_{t} experienced by the ions is expressed by the sum of a time-independent pseudopotential Φ_{ps} and a static potential Φ_{dc}:

$$\begin{aligned}\Phi_{\mathrm{t}} &= \Phi_{\mathrm{ps}} + \Phi_{\mathrm{dc}} \\ &= \frac{Q^2 V_{\mathrm{RF}}^2}{4M\Omega_{\mathrm{RF}}^2} \| \nabla \Phi_{\mathrm{RF}} \|^2 + Q \sum_i^n V_i \Phi_{\mathrm{dc},i}. \end{aligned} \quad (1)$$

Here, M and Q are the mass and charge of the trapped ions, respectively, and V_{RF} and Ω_{RF} denote the RF amplitude and frequency, respectively. Φ_{RF} denotes the RF-electrode-potential basis function. The results of the FEM calculations for $^{40}Ca^+$ are presented in figure 2 using $V_{\mathrm{RF}} =$ 495 V, $\Omega_{\mathrm{RF}} = 2\pi \times$ 8.0 MHz and $V = \{V_1, V_2, \ldots, V_{12}\} = \{2.35, 2.35, 21.5, 21.5, -6.0, -6.0, -6.6, -6.6, -6.0, -6.0, 23.0, 23.0\}$ V which correspond to typical operating parameters in our experiments. This configuration of static voltages optimized the total trap depth while generating 'axialized' crystals: the center of the crystal coincided with both the RF null line

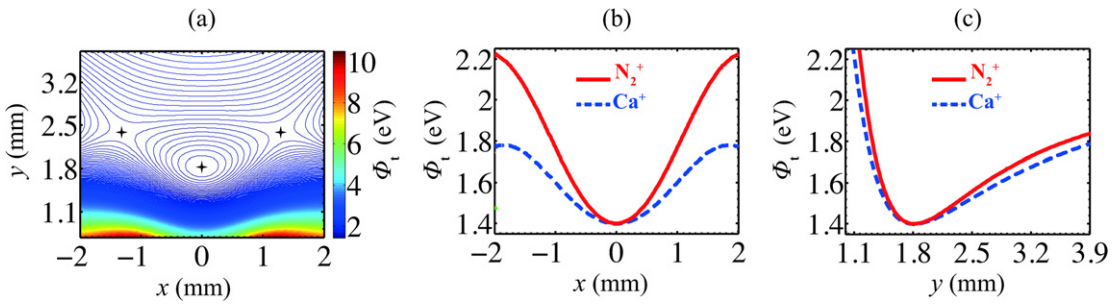

Figure 2. (a) Total trapping potential Φ_t for Ca^+ as a sum of pseudopotential and static potential in the (x, y) plane perpendicular to the RF null line intersecting the trap center. The crosses show the position of the potential minimum and the saddle points through which ions can escape the trap. (b), (c) One-dimensional cuts through Φ_t along the x and y axes for N_2^+ and Ca^+ illustrating the mass dependence of the trapping potential.

Table 1. Stability parameters for Ca^+ and N_2^+ under typical trap operating conditions.

	Q_{xx}	Q_{yy}	Q_{zz}	A_{xx}	A_{yy}	A_{zz}
$^{28}N_2^+$	0.1178	−0.1152	-5×10^{-4}	-22×10^{-4}	16×10^{-4}	6×10^{-4}
$^{40}Ca^+$	0.0824	−0.0806	-3×10^{-4}	-16×10^{-4}	11×10^{-4}	4×10^{-4}

and the minimum of the static potential Φ_{dc} in order to minimize excess micromotion [32]. The depth of the trap, defined as the difference in the total potential between the minimum and the two off-center saddle points through which ions can escape the trap (see figure 2(a)), was calculated to be 117 meV for Ca^+.

Using the same trapping parameters, the total potential Φ_t has been calculated for N_2^+ ions. Because of the inverse mass dependence of Φ_{ps}, the lighter ions experience a stronger confining force from the RF field leading to a segregation of the ion species in bicomponent Coulomb crystals [1, 16, 44]. The effective trap depth for N_2^+ ions was calculated to be 261 meV. Figures 2(b) and (c) show one-dimensional cuts of the effective potentials along the x and y axes for Ca^+ and N_2^+.

In table 1, the multidimensional generalization of the Mathieu stability parameters [31] for the present trap calculated for the operating parameters are given:

$$A_{ij} = \frac{4Q}{M\Omega_{RF}^2}\left(\frac{\partial^2\Phi_{dc}}{\partial x_i \partial x_j}\right), \qquad Q_{ij} = \frac{2Q}{M\Omega_{RF}^2}\left(\frac{\partial^2\Phi_{RF}}{\partial x_i \partial x_j}\right). \tag{2}$$

Here, the x_i $(i = 1, 2, 3)$ stand for the three spatial coordinates x, y and z. Stable operating conditions are achievable if $|Q_{ii}| \ll 1$ for both species [32, 45]. In comparison to linear Paul traps in which $A_{xx} = A_{yy} = -0.5A_{zz}$, the values for the A_{ii} can be more easily engineered in SE traps in order to shape the Coulomb crystals. The negative values for A_{xx} in table 1 imply that the static voltages have effectively reduced the total trapping force in the x direction. $A_{yy} > 0$ implies a tighter trap in the y (vertical) direction. This effect is generated by the potential of the endcap electrodes which, besides providing confinement along the trap axis $(A_{zz} > 0)$, also stiffen Φ_t in the vertical direction and weaken it along the x axis. As a result, the degeneracy of the radial modes of the ion motion is broken giving rise to non-spheroidal Coulomb crystals [29, 33]. This is of importance for shaping Coulomb crystals for potential applications in quantum computation and quantum simulation [46].

3. MD simulations

MD simulations were used to characterize the structures and energies of the Coulomb crystals obtained in the present study. MD simulations have been widely used for theoretically studying Coulomb crystals in Paul and Penning traps [34, 47–49]. Here, we briefly describe the adaptation of this technique to SE traps.

In our treatment, the following classical equations of motion for the laser- and sympathetically cooled ions are solved:

$$M_i\ddot{\mathbf{r}}_i = F_{i,\mathrm{Total}}(\mathbf{r}_1, \ldots, \mathbf{r}_{N_{\mathrm{atoms}}+N_{\mathrm{molecules}}}) = \mathbf{F}_{\mathrm{Trap}} + \mathbf{F}_{\mathrm{Coulomb}} + \mathbf{F}_{\mathrm{Heating}} + \mathbf{F}_{\mathrm{LC}} + \mathbf{F}_{\mathrm{RP}}, \quad (3)$$

Here, M_i and $\mathbf{r}_i$ are the mass and the position of the ith ion, respectively, and $i = 1, \ldots, N_{\mathrm{atoms}} + N_{\mathrm{molecules}}$ where N_{atoms} and $N_{\mathrm{molecules}}$ denote the number of the atomic and molecular ions, respectively. The contributions to the total force, as expressed by equation (3), are: the trapping force $\mathbf{F}_{\mathrm{Trap}}$, the Coulomb force between ions $\mathbf{F}_{\mathrm{Coulomb}}$, a stochastic heating force $\mathbf{F}_{\mathrm{Heating}}$, the laser cooling force $\mathbf{F}_{\mathrm{LC}}$ and the radiation pressure force $\mathbf{F}_{\mathrm{RP}}$ [47]. The first three terms act on both the atomic and molecular ions whilst the last two terms act only on the atomic ions. The sympathetic cooling is provided by the Coulomb interactions between the ions. Heating effects arise from experimental imperfections and are modeled as random force kicks on the ions. The Doppler laser cooling force is modeled as a friction force [50].

The properties of the Coulomb crystals depend on the trapping force which is in turn dependent on the geometry of the trap as well as the operating parameters. The trapping force $\mathbf{F}_{\mathrm{Trap}}$ was calculated from analytical gradients of the trapping potentials approximated by power series expansions of both static and RF potentials near the trap center (x_0, y_0, z_0):

$$\mathbf{F}_{\mathrm{Trap}}(x, y, z, t) = -\nabla\left(V_{\mathrm{RF}}\cos(\Omega t)\sum_{k,l,m} C_{\mathrm{RF}_{(k,l,m)}}(x-x_0)^k(y-y_0)^l(z-z_0)^m + \sum_{i=1}^{n} V_i \sum_{k,l,m} C_{\mathrm{dc},i_{(k,l,m)}}(x-x_0)^k(y-y_0)^l(z-z_0)^m\right). \quad (4)$$

$C_{\mathrm{RF}_{(k,l,m)}}$ ($C_{\mathrm{dc},i_{(k,l,m)}}$) is the coefficient of the (k, l, m)th order term in the RF (ith dc electrode) potential. The coefficients C_{RF} and $C_{\mathrm{dc},i}$ were obtained by three-dimensional fits to a series expansion truncated at 4th order to the numerically calculated potentials Φ_{RF} and Φ_{dc} (see equation (1)) in a cube with 400 μm side length around the trap center. As expressed by equation (4), the fully time-dependent trapping force was used in the simulations to account for micromotion effects [32]. The integration time step was 4.2 ns (1/30 RF period) while the typical simulation time interval was 3.75 ms.

The ion trajectories obtained from the simulations were used to reconstruct the experimental images. An iterative comparison between the experimental and simulated images was used to determine the ion numbers and kinetic energies in the experiments [1, 36, 47]. The secular temperature of the ions has a strong effect on the diffusion of the ions in the crystals and therefore on the contrast of the crystal structure observed in the images. The secular temperature of the ions in the experiment was determined by adjusting the temperature in the simulations through varying the magnitude of the heating force $\mathbf{F}_{\mathrm{Heating}}$ in equation (3) until the best match between the experimental and simulated images was reached. The total ion kinetic energies including the secular and micromotion energies were subsequently derived from the ion trajectories [47].

4. Results and discussion

First results were already reported in our previous study in which we presented shapes of bicomponent crystals obtained for light and heavy sympathetically cooled ions in the SE trap [29]. Here, we focus on three further aspects: (i) the shape and energetics of the bicomponent crystals as a function of the crystal composition, (ii) details of the experiments, already briefly introduced in [29], to spatially separate the different ion species in the crystals, and (iii) the effect of trap anharmonicities on the crystal shapes. In the present context, spatial separation refers to increasing the mean distance of the centers of the atomic and the molecular ion crystals, as opposed to the segregation of the ion species within perfectly axialized crystals [1, 44].

4.1. Structure and energetics of bicomponent crystals as a function of their composition

The number of sympathetically cooled N_2^+ ions in the crystals was controlled by varying the ionization rate of neutral N_2 following the preparation of a pure Ca^+ crystal. A set of experiments performed by loading varying numbers of N_2^+ ions into the trap is shown in figure 3. The molecular ions appear as a dark area in the center of the crystals and have been made visible in green in the simulations for clarity. Slight discrepancies between the experimental and simulated images are attributed to machining imperfections of the trap electrodes which were not accounted for in the simulations. The crystals in the experiments shown in figures 3(ii)–(vi) were composed of 3 up to 28% of N_2^+ ions as deduced from comparisons with simulated images. The uncertainty in the determination of the ion numbers amounted to ±1 for N_2^+ ions and ±2 (±5) for Ca^+ ions in small (big) crystals. The uncertainties arise from the fact that usually a range of simulated images with slightly varying ion numbers closely match the experimental image [36, 47]. The asymmetric structure of the N_2^+ crystals along the z axis resulted from the radiation pressure force acting on the Ca^+ ions caused by unidirectional laser cooling as well as

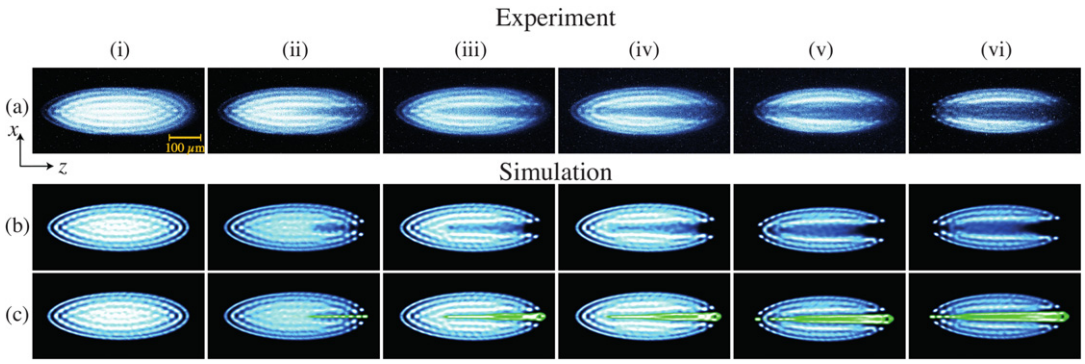

Figure 3. (a) Experimental and (b), (c) simulated false-color laser-cooling fluorescence images of Ca^+/N_2^+ bicomponent Coulomb crystals in the SE trap. In (c), the sympathetically cooled molecular ions were made visible in the simulations for clarity. Color code: Ca^+ = blue, N_2^+ = green. (i)–(vi) The Coulomb crystals shown in (i)–(vi) contained 0, 8, 22, 28, 42 and 50 N_2^+ ions corresponding to percentages of 0, 3, 9, 12, 22, 28% of the total number of ions.

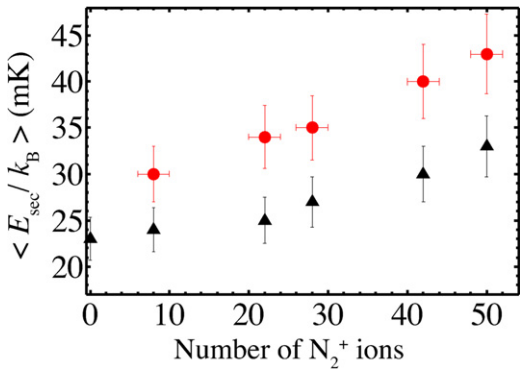

Figure 4. Average secular energies of laser-cooled atomic (Ca^+ = black triangle) and sympathetically cooled molecular (N_2^+ = red circle) ions plotted as a function of the number of sympathetically cooled N_2^+ ions in the crystals shown in figure 3.

asymmetries in the RF force caused by the asymmetric geometry of the finite-sized RF electrodes. During the loading phase, a small number of Ca^+ ions was lost because of collisions with neutral N_2 molecules.

The secular energies (i.e., the ion energies without micromotion) of the ions in the crystals of figures 3(i)–(vi) are shown in figure 4. The final ion energies depend on the number of laser-cooled ions in relation to the number of sympathetically cooled ions. Increasing the number of N_2^+ ions resulted in higher average secular energies for both species. For instance, the crystal shown in figure 3(ii) contains eight sympathetically cooled N_2^+ ions at $E_{sec}/k_B = 30$ mK in conjunction with 257 Ca^+ ions at $E_{sec}/k_B = 24$ mK. For the crystal in figure 3(vi), the average secular energy amounts to $E_{sec}/k_B = 43$ mK for 50 sympathetically cooled N_2^+ ions with 180 Ca^+ ions at $E_{sec}/k_B = 33$ mK. Across the series of crystals studied, the difference in average energy between the two species increased from 6 to 10 mK with increasing N_2^+ / Ca^+ ratio.

The trends observed in figure 3 can be explained by an increasingly unfavorable ratio of heating to cooling forces acting on the entire ion ensemble. As the molecular ions are only indirectly cooled by the Ca^+ ions, but are subject to the same heating processes (apart from photon recoil), the average secular energy of the N_2^+ ions is higher relative to the Ca^+ ions. The final secular temperature of both species depend both on the absolute and relative numbers of different ions in the crystal. These results are in harmony with previous findings on bicomponent crystals in linear Paul traps [17].

4.2. Spatial separation of the ion species

If a trapped ion is subjected to a uniform static electric field $\mathbf{E}_{dc}$ along the y axis, the average position of a single ion is displaced by $y_{ion} \cong Q\mathbf{E}_{dc} \cdot \hat{\mathbf{y}} / M\omega_i^2$ [32], where, ω_i is the secular frequency and $\hat{\mathbf{y}}$ the unit vector along y. Ions with different masses exhibit different displacements due to the mass dependence of the pseudopotential although they are subjected to the same static field. In large bicomponent Coulomb crystals, such displacements can result in a complete separation of the species if the difference between the displacements for each species exceeds the spatial extension of the crystals.

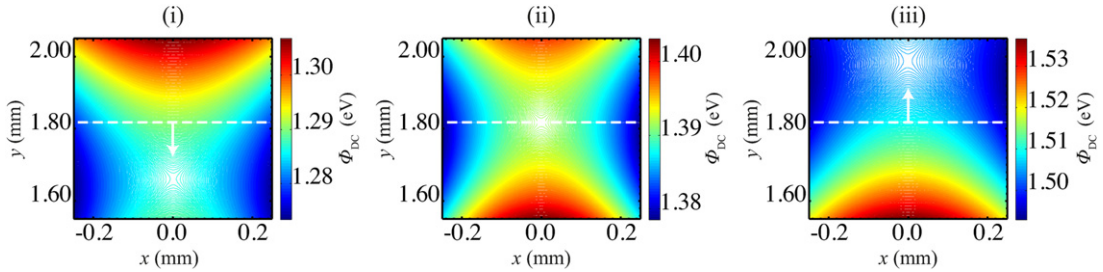

Figure 5. Static potential configurations Φ_{dc} in the (x, y) plane used for the spatial separation of the N_2^+ and Ca^+ ions. The dashed line indicates the position of the RF null line. In (i) and (iii), the minimum of the static potential was displaced below and above the RF null line, respectively. In (ii), the minimum of Φ_{dc} coincides with the RF null line, corresponding to an axialized trapping configuration.

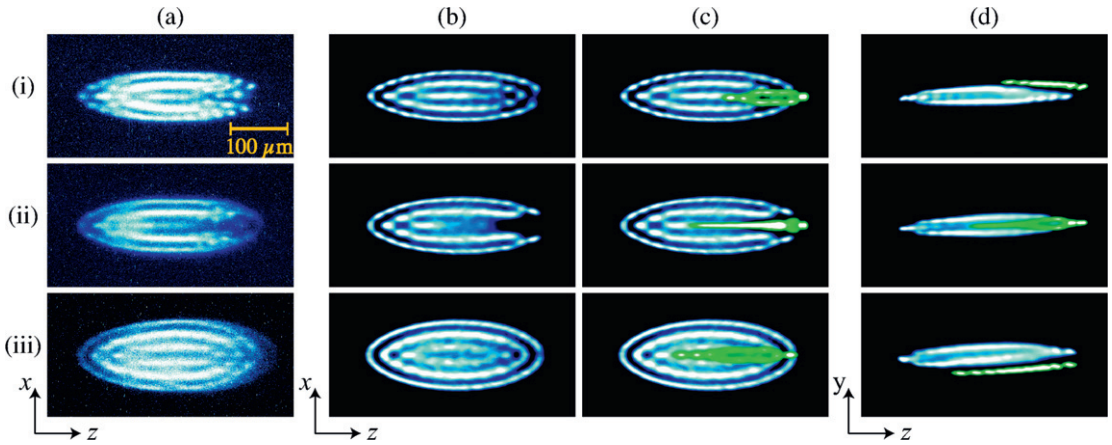

Figure 6. Demonstration of the spatial separation of Ca^+/N_2^+ Coulomb crystals into an atomic and molecular component. (a) Experimental and (b)–(d) simulated false-color fluorescence images. In (c), (d), the sympathetically cooled molecular ions were made visible in green in the simulations for clarity. In (d), side views of the simulated crystals are displayed showing the separation of the ion species. (i) The N_2^+ crystal was placed above the Ca^+ crystal while both were subjected to an electric field along the $-y$ direction and pushed underneath the RF null line. (ii) The crystal was axialized and the N_2^+ and Ca^+ crystals were centered on the RF null line. (iii) The N_2^+ crystal was placed underneath the Ca^+ crystal while both were subjected to an electric field along the $+y$ direction and pushed above the RF null line.

The static potential configurations used for demonstrating the spatial separation of the ions are shown in figure 5. By applying additional voltage offsets of −0.3, 0.0 and 0.35 V on the two central electrodes, the height of the trap minima for both species was changed. The static fields generated along the y axis were calculated to be 46 V m^{-1}($-\hat{y}$), 0 V m^{-1}, 50 V m^{-1}($+\hat{y}$) at the center of the trap across the three configurations shown in figures 5(i)–(iii). Figures 6(i)–(iii) show a Coulomb crystal obtained under these three trapping conditions. In figures 6(i) and (iii), a near-planar bicomponent crystal is shown in which the N_2^+ ions were spatially separated from the Ca^+ ions in the positive and negative y directions, respectively. In figure 6(ii) the same crystal was centered on the RF null line.

Figure 7(a) shows the extent of the spatial separation of the species in the experiments of figure 6 as extracted from the MD simulations. In the crystal shown in figure 6(i), the average displacements from the RF null line $\langle y_{ion} \rangle$ were obtained to be 50 μm for N_2^+ and 31 μm for Ca^+ leading to a separation of 19 ± 2 μm. By pushing the ions above the RF null line as shown in figure 6(iii), the layers of N_2^+ and Ca^+ ions were moved by 40 and 62 μm, respectively, resulting in an average separation of 22 ± 2 μm.

As shown in figure 7(b), the spatial separation of the sympathetically cooled N_2^+ ions from the laser-cooled Ca^+ ions adversely affected the cooling efficiency owing to the reduced contact volume between the two species. Moreover, the application of the uniform static field not only changed the height of trapping, but also the secular frequencies. This can also be seen from the variation of the aspect ratios of the crystals in figures 6(a) (i)–(iii). The secular frequencies for Ca^+ were calculated to be $(\omega_x, \omega_y, \omega_z) = (186, 290, 83)$, (172, 273, 83) and (156, 257, 84) kHz for the crystals shown in figures 6(i)–(iii), respectively. Consequently, the secular kinetic energies of the

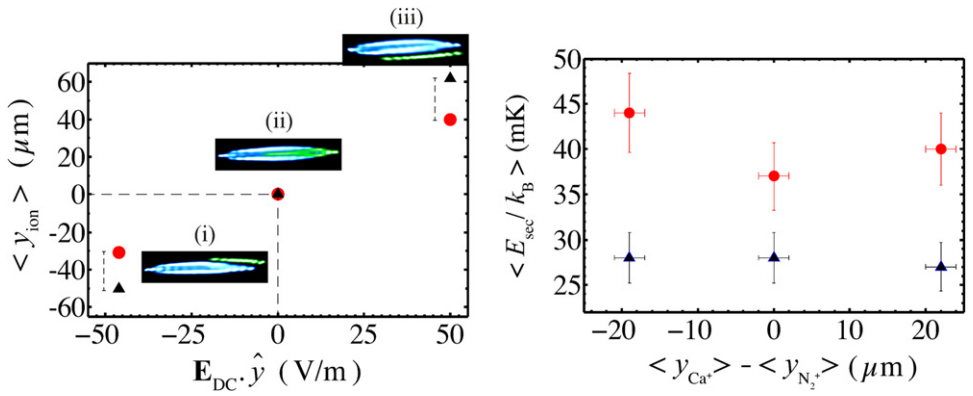

Figure 7. (a) Shifts of the average ion positions $\langle y_{ion} \rangle$ for Ca^+ and N_2^+ caused by an applied static field (Ca^+ = black triangle, N_2^+ = red circle) for the three crystals shown in figure 6. The error bars in the distances are smaller than the size of the symbols. (b) Average secular energies of both species as a function of distance between the atomic and molecular ions. The error bars reflect the uncertainties in the comparison of the simulated with the experimental images.

Ca^+ ions $E_{Kin(i)} \propto M u_{(i)} \omega_i^2$ (where $u_{(i)}$ is the amplitude of the relevant ion's secular motion [32]) were also modified.

The static electric fields used to separate the ion species caused significant excess micromotion in both species. The Ca^+ ions were subjected to wider micromotion amplitudes because of their farther displacements from the RF null line. We inferred that the average total energies of the ions have been increased by $\Delta E_{total}/k_B = 3.5$ K for N_2^+ and $\Delta E_{total}/k_B = 7$ K for Ca^+ ions in the case for the crystal pushed underneath the RF null line in figure 6(i). For the crystals pushed above the RF null line in figure 6(iii), $\Delta E_{total}/k_B = 4.5$ and 13.5 K have been calculated for the N_2^+ and Ca^+ ions, respectively. The higher energies compared to the conditions in figure 6(i) were caused by the farther displacement of the ions from the RF null line in this case.

4.3. Effects of trap anharmonicity

The low symmetry of SE traps leads to significant anharmonic contributions to the trapping potential. Anharmonicity effects can become particularly significant in experiments with a large number of trapped ions. For instance, in large Coulomb crystals in anharmonic traps, different ions may experience different curvatures of the trapping potential owing to their different equilibrium positions.

The effects of anharmonicity can be quantified in the framework of a power series expansion [51]:

$$\Phi_t(x_i) = \sum_{n=2}^{\infty} \kappa_n x_i^n = \kappa_2 x_i^2 \left[1 + \sum_{n=3}^{\infty} \left(\frac{x_i}{\lambda_n} \right)^{n-2} \right], \tag{5}$$

where here, Φ_t refers to a one-dimensional cut through the total potential, κ_n are expansion coefficients and $\lambda_n = (\kappa_n/\kappa_2)^{1/(2-n)}$ parametrizes the length scale over which anharmonic terms of order n become comparable to the harmonic contribution. The larger λ_n, the less significant the corresponding anharmonic potential term and the longer the length scale over which anharmonicity manifests itself in the properties of the ion crystals.

Anharmonicity can have pronounced effects on the structure of bicomponent crystals in SE traps as already explored in a preliminary theoretical study [52]. As implied by equation (5), anharmonic terms tend to be more pronounced in small traps which exhibit small values of λ_n (unless the potentials are especially tailored to suppress or engineer anharmonic contributions [53, 54]). The question therefore arises at which size of trap anharmonicities start to appreciably affect the properties of bicomponent crystals.

In order to address this issue, we have simulated bicomponent crystals in five-wire SE traps of different sizes. As the height of trapping is determined by the size of the electrode structures [31, 42], we chose the height of trapping as the characteristic length scale for the systems. We used the Surface Pattern software [38] to design traps with a specific trapping height and to model their trapping potentials. The resulting SE geometries were refined using the analytical model from [31]. The geometries of these traps were $(a,\ b,\ h) = (1975, 2332, 1800)$, $(979, 1166, 900)$, $(544, 648, 500)$, $(217, 259, 200)$ and $(109, 129, 100)$ μm, where a and b are the width of the central and the two RF electrodes, respectively, and h is the trapping height. The applied RF and static voltages were chosen such that the harmonic trap frequencies were kept the same in all cases ($\omega_y = \omega_x = 840$ kHz and $\omega_z = 300$ kHz) in order to render the harmonic part of the trap potentials comparable and keep the radial frequencies degenerate to enable a comparison with linear Paul traps [1]. Thus, the RF frequency $\Omega_{RF} = 2\pi \times 8.17$ MHz and the A_{ii} and Q_{ii} parameters (see equation (2)) were the same for all traps. Figure 8(a) shows cuts

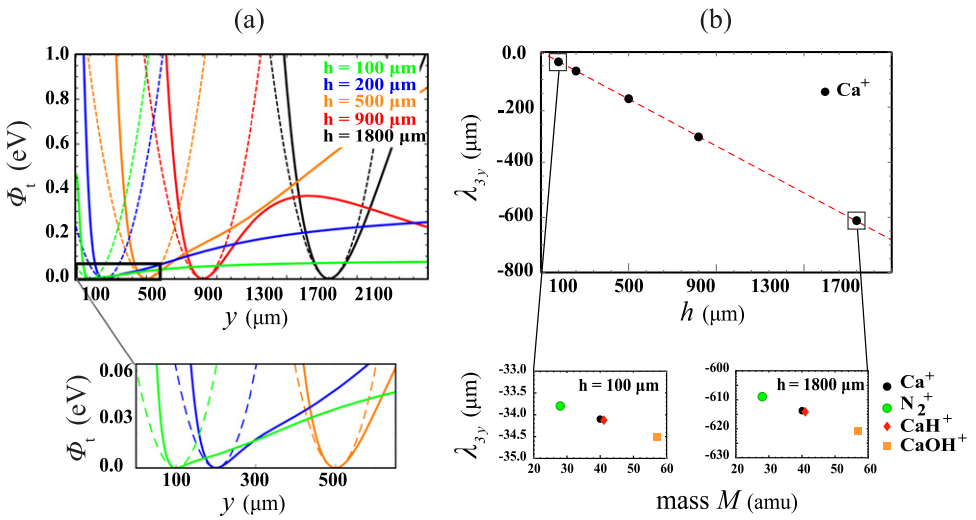

Figure 8. (a) One-dimensional cuts through the total trapping potential Φ_t for Ca^+ along the vertical (y) axis through the trap center for SE traps with different trapping heights h and identical harmonic frequencies (solid lines). The dashed lines show a harmonic potential yielding the same secular frequencies. The inset shows a magnified view of the potentials near the trap center of the smallest traps. (b) Anharmonicity parameter along the y axis λ_{3y} for the same traps. The insets show λ_{3y} for different ion species in the traps with $h = 100$ and 1800 μm.

through the total potential Φ_t along the vertical (y) axis for the different traps obtained under these conditions (solid lines). For comparison, the dashed lines represent a harmonic potential with the same harmonic trapping frequencies. The inset shows a magnification of the potentials near their minima for the smallest three traps.

Already a visual comparison of Φ_t with the harmonic potential illustrates the increasing degree of anharmonicity with decreasing trap size. This is quantified in figure 8(b) which shows λ_{3y}, the λ_3 parameter for Φ_t along the y axis, obtained by a fit of equation (5) to Φ_t. λ_{3y} scales linearly with the trapping height (as can also be shown from equation (5)) ranging from -34 μm to -614 μm for the smallest to the largest trap studied, respectively. The insets show λ_{3y} for different molecular-ion species. The mass dependence of λ_{3y} results from the slightly different strengths of the pseudopotential Φ_{ps} for the different species (see equation (1)).

In figures 9(a)–(d), MD simulations of bicomponent crystals containing 50 Ca^+ ions and ten sympathetically cooled ions for three different molecular species in SE traps of four different sizes (labeled by their trapping heights h) are presented. The ions form spheroidal crystals with spatial extensions <30 μm in the (x, y) plane. The panels show 'snapshots' of ion configurations obtained near the end of the simulation period. For comparison, the analogous crystals obtained in a large linear Paul trap with the same harmonic secular frequencies are shown in figure 9(e). The only weakly anharmonic, larger SE traps exhibit crystal structures resembling the ones in the linear Paul trap. By contrast, the more anharmonic, smaller traps show an asymmetric segregation of the ion species which becomes more pronounced with decreasing trap size. This asymmetric segregation is a consequence of the increasingly anharmonic trap potential in the vertical direction for smaller traps as shown in figure 8(a). This effect is particularly pronounced for heavy sympathetically cooled ions like $CaOH^+$ (see bottom panel in figure 9) with comparatively week pseudopotentials in the vertical direction. We note that special care was taken to ensure that the minima of Φ_t and Φ_{ps} coincided for all crystals in order to avoid artifacts in the simulations resulting from imperfect axialization. In the previous theoretical study [52], the effects of anharmonicity discussed here were already observed in a trap with a trapping height $h \approx 900$ μm. The anharmonic effects were, however, amplified by an inadequate parametrization of the static potential in that study. Based on the present results, we estimate that appreciable effects on the crystal shapes will be noticeable in traps with structures which are at least a factor of two to three smaller than the one studied in [52] (see figure 9).

The effects described above relate to the strength of anharmonic terms as a function of the size of the SE structures at fixed harmonic frequencies. One should also note that such effects also depend on the trapping conditions, e.g., RF frequency and amplitudes, as well as static control fields. These have not been characterized in the present study. In fact, anharmonicities can be introduced deliberately using tailored control fields to engineer ion crystals with special properties [54].

The average total kinetic energies of the Coulomb-crystallized ions shown in figure 9 are displayed in figure 10. The total kinetic energies are dominated by the contribution from the ion micromotion and therefore from their distance from the RF null line. The energies of the different ion species are essentially the same in the

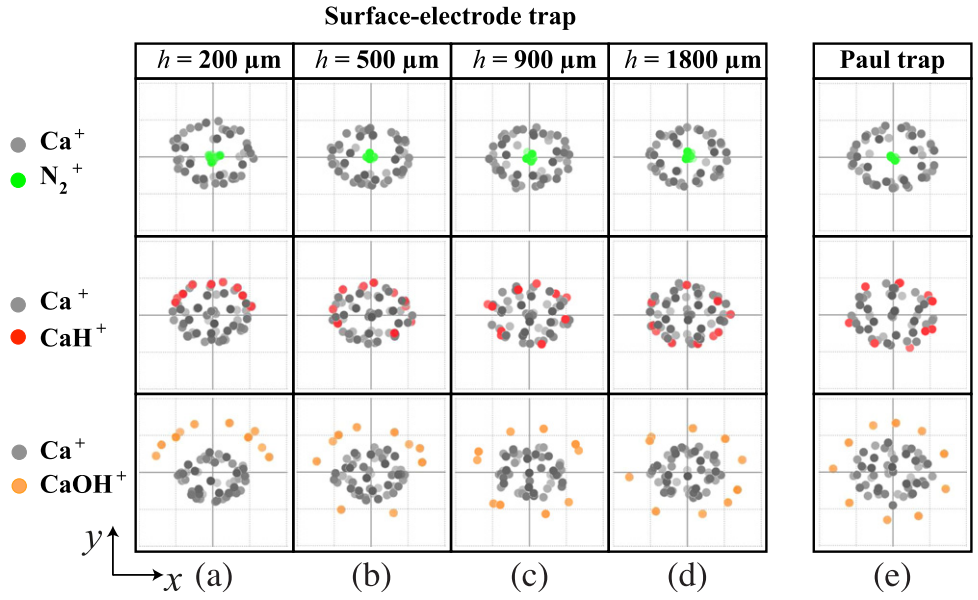

Figure 9. (a)–(d) MD simulations of bicomponent crystals containing 50 Ca^+ ions and ten molecular ions in SE traps with different trapping heights from figure 8. The figures show snapshots of the ion positions viewed along the z axis and taken near the end of the simulation period. The λ_{3y} values calculated for trapping potentials in (a)–(d) are −68, −107, −307, −614 μm, respectively. (e) For comparison, the same crystals have also been simulated in a linear Paul trap. The vertical and horizontal lines in the figures indicate separations of 10 μm.

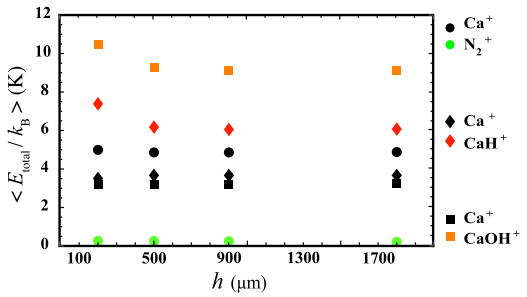

Figure 10. Average total kinetic energies of the Coulomb-crystallized ions in SE traps with different trapping heights shown in figure 9.

traps with $h = 900$ and 1800 μm. As these traps can essentially be regarded as harmonic for the sizes of the crystal of figure 9, the total ion kinetic energies are only weakly affected by potential anharmonicities. On the other hand, for the smaller traps with $h = 500$ μm and 200 μm, an increase in the ion energies can be observed particularly for heavy sympathetically cooled species. This effect is a ramification of the increasing role of anharmoncity with decreasing trap size which forces the heavy sympathetically cooled species to disclocate farther from the RF null line (as can clearly be seen, for instance, in figure 9(a) for $CaOH^+$) and therefore assume wider micromotion amplitudes.

The characteristics of the comparatively large trap used in the present experiments were similar to the one with trapping height $h = 1800$ μm characterized in figures 8–10. Anharmonicity parameters as defined in equation (5) were calculated from power series fitted to one-dimensional cuts through the total potential $\Phi_t(x_i)$ in a region of 400 μm around the trap center. The parameters along the y axis were obtained to be $\lambda_{3y} = -750$ μm and $\lambda_{4y} = 890$ μm. The anharmonicity parameters along the x and z axes were about two orders of magnitude larger. Moreover, the trapping conditions used in the experiments resulted in Coulomb crystals with typical extensions <100 μm along the most anharmonic direction (y) so that anharmonic effects did not play a role in our experiments. This is illustrated in figure 11 which illustrates the region of validity of the harmonic approximation for the present trap in relation to the size of a typical large crystal in our SE trap. Thus, for practical purposes the trap used in the present study can be regarded to be harmonic in a good approximation.

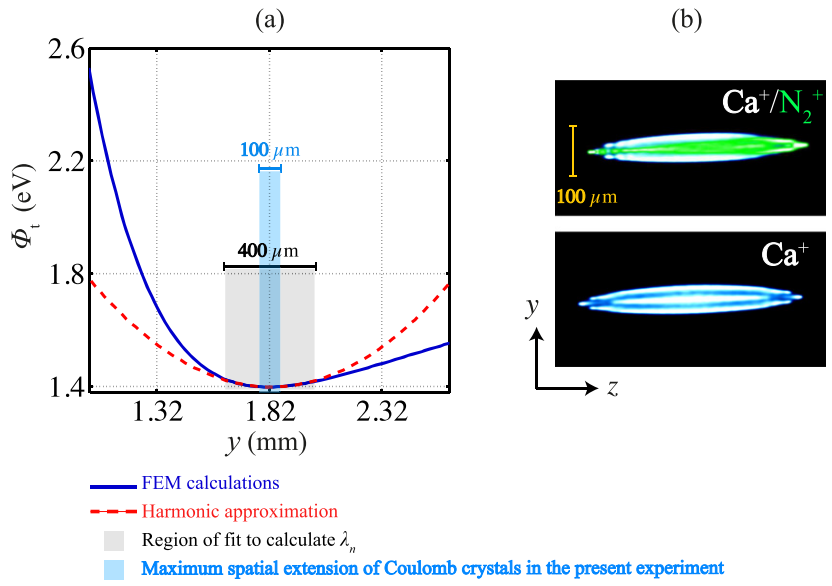

Figure 11. (a) Validity of the harmonic approximation in the present SE trap. (a) One-dimensional cut through the total potential Φ_t for Ca^+ ions along the vertical (y) direction near the trap center. The anharmonicity parameters λ_n and trapping force coefficients were calculated in a region of 400 μm around the trap center. (b) Side view of a typical large crystal containing 262 Ca^+ ions (bottom), 180 Ca^+ and 50 N_2^+ ions (top) showing a maximum spatial extension <100 μm along the vertical direction.

5. Summary and conclusions

In the present study, we have investigated the structural and energetic properties of bicomponent Coulomb crystals in a SE ion trap. Crystal shapes and the ion energies were characterized by comparisons of experimental laser-cooling fluorescence images with MD simulations. Methods for spatially separating the ion species in our experiments using static control fields were detailed and the effect of the separation on the crystal shapes and the ion energies were discussed. The effects of trap anharmonicities on the shapes and energies of bicomponent crystals were explored. It was concluded that anharmonicities appreciably affect the crystal properties in small to medium-sized traps when the spatial extension of the ions becomes comparable to the smallest anharmonicity parameter, but can be neglected in large, mm-sized traps such as the one used in our experiments. On the other hand, the trapping potentials can also deliberately be engineered to spatially separate ion species in bicomponent crystals, as demonstrated in the present study.

In conclusion, we have shown that SE traps represent versatile tools for experiments with cold molecular ions. The chief advantage of the SE structure lies in the flexibility, scalability and variability of the electrode layouts which allow to accurately shape trapping potentials. Therefore, SE trapping architectures have the potential to become useful devices for a range of molecular applications ranging from highly integrated ion experiments to the development of hybrid quantum systems.

Acknowledgments

We gratefully acknowledge the technical support by Dieter Wild, Grischa Martin, Philipp Knöpfel, Andreas Tonin and Dr Anatoly Johnson. A M thanks Dr Iulia Georgescu for helpful discussions and for suggesting the method of manufacturing the SE trap. This work has been supported by the University of Basel, the COST Action MP1001 'Ion Traps for Tomorrow's Applications', the Swiss National Science Foundation through the National Centre of Competence in Research 'Quantum Science and Technology' and the Swiss Nanoscience Institute.

References

[1] Willitsch S 2012 *Int. Rev. Phys. Chem.* **31** 175
[2] van de Meerakker S Y T, Bethlem H L, Vanhaecke N and Meijer G 2012 *Chem. Rev.* **112** 4828
[3] Carr L D, DeMille D, Krems R V and Ye J 2009 *New J. Phys.* **11** 055049
[4] DeMille D 2002 *Phys. Rev. Lett.* **88** 067901
[5] Mur-Petit J, Pérez-Ríos J, Campos-Martínez J, Hernández M I, Willitsch S and García-Ripoll J J 2012 *Phys. Rev.* A **85** 022308
[6] Koelemeij J C J, Roth B and Schiller S 2007 *Phys. Rev.* A **76** 023413

[7] Germann M, Tong X and Willitsch S 2014 *Nat. Phys.* **10** 820
[8] Schuster D I, Bishop L S, Chuang I L, DeMille D and Schoelkopf R J 2011 *Phys. Rev.* A **83** 012311
[9] Drewsen M, Mortensen A, Martinussen R, Staanum P and Sorensen J L 2004 *Phys. Rev. Lett.* **93** 243201
[10] Staanum P F, Højbjerre K and Drewsen M 2010 *Practical Aspects of Trapped Ion Mass Spectrometry* vol 5 (Boca Raton, FL: CRC Press) p 291
[11] Willitsch S, Bell M T, Gingell A D, Procter S R and Softley T P 2008 *Phys. Rev. Lett.* **100** 043203
[12] Ospelkaus S, Ni K-K, Wang D, de Miranda M H G, Neyenhuis B, Quéméner G, Julienne P S, Bohn J L, Jin D S and Ye J 2010 *Science* **327** 853
[13] Hall F H J and Willitsch S 2012 *Phys. Rev. Lett.* **109** 233202
[14] Kirste M, Wang X, Schewe H C, Meijer G, Liu K, van der Avoird A, Janssen L M C, Gubbels K B, Groenenboom G C and van de Meerakker S Y T 2012 *Science* **338** 1060
[15] Shuman E S, Barry J F and DeMille D 2010 *Nature* **467** 820
[16] Mølhave K and Drewsen M 2000 *Phys. Rev.* A **62** 011401
[17] Ostendorf A, Zhang C B, Wilson M A, Offenberg D, Roth B and Schiller S 2006 *Phys. Rev. Lett.* **97** 243005
[18] Hansen A K, Versolato O O, Klosowski L, Kristensen S B, Gingell A, Schwarz M, Windberger A, Ullrich J, Crespo Lopez-Urrutia J R and Drewsen M 2014 *Nature* **508** 76–79
[19] Hughes M D, Lekitsch B, Broersma J A and Hensinger W K 2011 *Contemp. Phys.* **52** 505–29
[20] Ospelkaus C, Warring U, Colombe Y, Brown K R, Amini J M, Leibfried D and Wineland D J 2011 *Nature* **476** 181
[21] Amini J M, Uys H, Wesenberg J H, Seidelin S, Britton J, Bollinger J J, Leibfried D, Ospelkaus C, VanDevender A P and Wineland D J 2010 *New J. Phys.* **12** 033031
[22] Kielpinski D, Monroe C and Wineland D J 2002 *Nature* **417** 709
[23] Home J P, Hanneke D, Jost J D, Amini J M, Leibfried D and Wineland D J 2009 *Science* **325** 1227
[24] Häffner H, Roos C F and Blatt R 2008 *Phys. Rep.* **469** 155
[25] Monroe C and Kim J 2013 *Science* **339** 1164
[26] Clark C R, Chou C, Ellis A R, Hunker J, Kemme S A, Maunz P, Tabakov B, Tigges C and Stick D L 2014 *Phys. Rev. Appl.* **1** 024004
[27] Chiaverini J, Blakestad R B, Britton J, Jost J D, Langer C, Leibfried D, Ozeri R and Wineland D J 2005 *Quantum Inf. Comput.* **5** 419
[28] Sterling R C, Rattanasonti H, Weidt S, Lake K, Srinivasan P, Webster S C, Kraft M and Hensinger W K 2013 *Nat. Commun.* **5** 3637
[29] Mokhberi A and Willitsch S 2014 *Phys. Rev.* A **90** 023402
[30] Allcock D T C, Sherman J A, Curtis M J, Imreh G, Burrell A H, Szwer D J, Stacey D N, Steane A M and Lucas D M 2010 *New J. Phys.* **12** 053026
[31] House M G 2008 *Phys. Rev.* A **78** 033402
[32] Berkeland D J, Miller J D, Bergquist J C, Itano W M and Wineland D J 1998 *J. Appl. Phys.* **83** 5025
[33] Szymanski B, Dubessy R, Dubost B, Guibal S, Likforman J P and Guidoni L 2012 *Appl. Phys. Lett.* **100** 171110
[34] Tong X, Wild D and Willitsch S 2011 *Phys. Rev.* A **83** 023415
[35] Jones R M, Gerlich D and Anderson S L 1997 *Rev. Sci. Instrum.* **68** 3357
[36] Tong X, Winney A H and Willitsch S 2010 *Phys. Rev. Lett.* **105** 143001
[37] COMSOL Multiphysics version 3.5a and 4.3a, www.comsol.com
[38] Schmied R 2013 *Surface Pattern software package* (https://atom.physik.unibas.ch/people/romanschmied/code/SurfacePattern.php)
[39] Schmied R, Wesenberg J H and Leibfried D 2009 *Phys. Rev. Lett.* **102** 233002
[40] Schmied R 2010 *New J. Phys.* **12** 023038
[41] Curtis M J 2010 *PhD Thesis* Universiy of Oxford
[42] Wesenberg J H 2008 *Phys. Rev.* A **78** 063410
[43] Gerlich D 1992 *Adv. Chem. Phys.* **82** 1
[44] Hornekær L, Kjærgaard N, Thommesen A M and Drewsen M 2001 *Phys. Rev. Lett.* **86** 1994
[45] Shaikh F A and Ozakin A 2012 *J. Appl. Phys.* **112** 074904
[46] Buluta I M, Kitaoka M, Georgescu S and Hasegawa S 2008 *Phys. Rev.* A **77** 062320
[47] Zhang C B, Offenberg D, Roth B, Wilson M A and Schiller S 2007 *Phys. Rev.* A **76** 012719
[48] Okada K, Wada M, Takayanagi T, Ohtani S and Schuessler H A 2010 *Phys. Rev.* A **81** 013420
[49] Dubin D H E and O'Neill T M 1988 *Phys. Rev. Lett.* **60** 511–4
[50] Metcalf H J and van der Straten P 1999 *Laser Cooling and Trapping* (New York: Springer)
[51] Home J P, Hanneke D, Jost J D, Leibfried D and Wineland D J 2011 *New J. Phys.* **13** 073026
[52] Georgescu I M and Willitsch S 2011 *Phys. Chem. Chem. Phys.* **13** 18852
[53] Schulz S, Poschinger U, Singer K and Schmidt-Kaler F 2006 *Fortschr. Phys.* **54** 648–65
[54] Lin G D, Zhu S L, Islam R, Kim K, Chang M S, Korenblit S, Monroe C and Duan L M 2009 *Europhys. Lett.* **86** 60004